HHS Public Access

Author manuscript

Sci Transl Med. Author manuscript; available in PMC 2020 December 18.

Published in final edited form as:

Sci Transl Med. 2019 December 18; 11(523): . doi:10.1126/scitranslmed.aay7162.

Biocompatible near-infrared quantum dots delivered to the skin by microneedle patches record vaccination

Kevin J. McHugh[1,#,†], **Lihong Jing**[1,2,#], **Sean Y. Severt**[1], **Mache Cruz**[1], **Morteza Sarmadi**[1,3], **Hapuarachchige Surangi N. Jayawardena**[1,‡], **Collin F. Perkinson**[4], **Fridrik Larusson**[5], **Sviatlana Rose**[1], **Stephanie Tomasic**[1], **Tyler Graf**[1], **Stephany Y. Tzeng**[1,§], **James L. Sugarman**[1], **Daniel Vlasic**[6], **Matthew Peters**[5], **Nels Peterson**[5], **Lowell Wood**[5], **Wen Tang**[1], **Jihyeon Yeom**[1], **Joe Collins**[1], **Philip A. Welkhoff**[7], **Ari Karchin**[5], **Megan Tse**[1], **Mingyuan Gao**[2], **Moungi G. Bawendi**[4], **Robert Langer**[1,*], **Ana Jaklenec**[1,*]

[1]Koch Institute for Integrative Cancer Research, Massachusetts Institute of Technology, 77 Massachusetts Avenue, Cambridge, MA 02139.

[2]Key Laboratory of Colloid, Interface and Chemical Thermodynamics, Institute of Chemistry, Chinese Academy of Sciences, Bei Yi Jie 2, Zhong Guan Cun, Beijing 100190, China.

[3]Department of Mechanical Engineering, Massachusetts Institute of Technology, 77 Massachusetts Avenue, Cambridge, MA 02139.

[4]Department of Chemistry, Massachusetts Institute of Technology, 77 Massachusetts Avenue, Cambridge, MA 02139.

[*]Corresponding author. rlanger@mit.edu (R.L.); jaklenec@mit.edu (A.J.).
[†]Current address: Department of Bioengineering, Rice University, Houston, Texas 77005.
[‡]Current address: Department of Chemistry, University of Alabama in Huntsville, Huntsville, AL 35899.
[#]These authors contributed equally to this work
[§]School of Medicine, Johns Hopkins University, 733 N. Broadway, Baltimore, MD 21205.

Author contributions: K.J.M., R.L., A.J., L.W., and P.A.W. devised the concept, K.J.M., L.J., R.L., and A.J. designed the experiments and wrote the manuscript. L.J. designed and synthesized quantum dots. L.J., H.S.N.J., C.F.P., and J.Y. performed optical characterization and analysis. M.G.B. and M.G. oversaw quantum dot synthesis and analysis. L.J., H.S.N.J., and W.T. performed Q.D. encapsulation. M.S. performed the computational modeling simulations. K.J.M., S.Y.S., and M.C. designed and fabricated microneedles. K.J.M., S.Y.S., C.F.P., F.L., M.P., N.P., and A.K. designed the smartphone optics. K.J.M., L.J., H.S.N.J., S.Y.S., S.Y.T., T.G., J.C., J.L.S., and M.T. performed the in vitro experiments. K.J.M., S.Y.S., and M.C. performed the ex vivo studies. K.J.M., S.Y.S., M.C., S.R., and S.T. performed the in vivo experiments and corresponding analysis. M.S. and D.V. developed the machine learning algorithm.

Supplementary Materials:
Materials and Methods
Fig. S1. Optical properties of organic dyes
Fig. S2. Evolution of fluorescence emission properties with shelling time
Fig. S3. Fluorescence lifetime characterization of the S10C QD series
Fig. S4. Composition and physical properties of S10C5H QDs
Fig. S5. pH stability of PMMA-encapsulated QDs
Fig. S6. Finite element analysis of mechanical forces on microneedles
Fig. S7. Optimization of microneedle geometry using finite element analysis
Fig. S8. Machine learning training and validation
Table S1. Characterization of custom synthesized quantum dots
Table S2. Multi-exponential fitting parameters for photoluminescent decay curves
Movie S1. Intradermal administration and imaging of encapsulated QDs
References (54–62)

Competing interests: A patent application entitled “Microneedle tattoo patches and use thereof” describing the approach presented here was filed by K.J.M., L.J., S.Y.S., H.S.N.J., A.J., and R.L. (US 62/558,172).

Data and materials availability: All data associated with this study are in the paper or supplementary materials. Computer code archived publicly accessible.

[5]Global Good, Intellectual Ventures Laboratory, 14360 SE Eastgate Way, Bellevue, WA 98007.

[6]Google, 355 Main St, Cambridge, MA 02142.

[7]Institute for Disease Modeling, 3150 139th Ave SE, Bellevue, WA, 98005.

Abstract

Accurate medical recordkeeping is a major challenge in many low-resource settings where well-maintained centralized databases do not exist, contributing to 1.5 million vaccine-preventable deaths annually. Here, we present an approach to encode medical history on a patient using the spatial distribution of biocompatible, near-infrared quantum dots (NIR QDs) in the dermis. QDs are invisible to the naked eye yet detectable when exposed to near infrared light. QDs with a copper indium selenide core and aluminum-doped zinc sulfide shell were tuned to emit in the NIR spectrum by controlling stoichiometry and shelling time. The formulation showing the greatest resistance to photobleaching after simulated sunlight exposure (5-year equivalence) through pigmented human skin was encapsulated in microparticles for use in vivo. In parallel, microneedle geometry was optimized in silico and validated ex vivo using porcine and synthetic human skin. QD-containing microparticles were then embedded in dissolvable microneedles and administered to rats with or without a vaccine. Longitudinal in vivo imaging using a smartphone adapted to detect in the NIR demonstrated that microneedle-delivered QD patterns remained bright and could be accurately identified using a machine learning algorithm nine months after application. Additionally, co-delivery with inactivated poliovirus vaccine produced neutralizing antibody titers above the threshold considered protective. These findings suggest that intradermal QDs can be used to reliably encode information and can be delivered with a vaccine, which may be particularly valuable in the developing world and opens up new avenues for decentralized data storage and biosensing.

One Sentence Summary:

Near-infrared fluorescent microparticles administered to the skin via dissolvable microneedle patches can record vaccine delivery.

Introduction

Vaccines are exceptionally safe and effective, saving an estimated 2–3 million lives annually (1). However, each year 1.5 million vaccine preventable deaths occur due to undervaccination—primarily in areas of the developing world with poor healthcare infrastructure (2). One key barrier to improving vaccination coverage in these regions is the inability to accurately identify the immunization status of infants given resource constraints, which can affect the quality of care provided (3,4). These areas often lack accurate medical recordkeeping systems and rely on vaccination campaigns to distribute vaccines. However, investigations in response to recent outbreaks of measles and mumps in the U.S. (5), Australia (6), and Italy (7), have highlighted that poor immunization recordkeeping is not unique to developing nations.

Paper vaccination cards or certificates are the most widely used records in the developing world, but are subject to error (8) and possessed by only 60% of all households in low-and

middle-income countries (9). Without accurate vaccination records, healthcare professionals lack the data to make informed decisions about administering vaccines, often relying on parental recall (10). This may result in the application of additional, unnecessary vaccine doses and therefore undue cost or, more problematically, missed opportunities to vaccinate, which leaves the child at risk for contracting infectious diseases (8,10). As many as two-thirds of opportunities to vaccinate may be missed in some areas (11), leading to a potential 30% drop in vaccination coverage (3). Several solutions have been proposed including smartphone-based database applications (12), fingerprinting (13), and near field communication chips (14); however, these more technologically advanced methods have yet to achieve widespread adoption due to difficulty of implementation.

Therefore, we aimed to develop a platform that is robust, inexpensive, and easy-to-use to overcome the primary obstacles to implementation in the developing world. We hypothesized that information, such as vaccination history, could be encoded invisibly in the skin by applying a distinct pattern of near-infrared (NIR) fluorescent microparticles using a microneedle patch. By providing all of the requisite information on the patients themselves, and delivering microparticles in the same microneedles as the vaccine, this platform offers several key advantages compared to traditional paper or electronic medical records including: i) the elimination of need for a widely-accessible, yet secure database of patient information; ii) lack of reliance on accurate patient identification and data entry by medical professionals; iii) ability to make rapid determinations of vaccination status; iv) elimination of vaccination fraud; v) capacity for population-level assessment of vaccine coverage; and vi) minimal cost that is feasible to implement in low-resource settings. By using a microneedle form factor, this platform should easily assimilate into the future vaccination landscape, since microneedles are currently in development for several vaccines (15) and have shown advantages such as antigen dose-sparing, improved antigen stability, and ease of (self-)administration compared to traditional soluble injections (16–18). Microneedle patches for vaccination recordkeeping may not require cold chain storage and could potentially have long shelf life, which could greatly enhance feasibility of implementation in low-resource settings.

Results

Commercial dye and custom quantum dot characterization

To create a microneedle platform that could be applied to the skin, rapidly dissolve, and leave behind particles that can later be imaged to determine vaccination status (Fig. 1, A–C), we first needed to identify a suitable candidate for long-term detection. We began by investigating the use of commercial fluorophores with emission in the NIR spectrum. To examine resistance to photobleaching, a key criterion for use in our application, fluorescent dyes were covered with pigmented cadaveric human skin and exposed to light simulating the solar spectrum at seven-fold higher intensity. Despite being heavily protected from light by overlying human skin, organic fluorophores photobleached within a few weeks of simulated sun exposure (Fig. 1D). Alternatively, inorganic commercial dyes demonstrated considerable resistance to photobleaching, but exhibited low fluorescence intensity per mass and were difficult to process due to their insolubility in both water and organic solvents. We then

pursued the use of colloidal quantum dots (QDs), also known as semiconductor nanocrystals, as potential fluorescent probes due to their favorable brightness and photostability. We synthesized and characterized more than 60 distinct combinations of $CuInSe_2$ cores and ZnS:Al shells (table S1). By changing the core stoichiometry and shell thickness, we could control the peak emission wavelength (Fig. 1E), enhance the photoluminescence quantum yield (PL QY) (Fig. 1F), and affect other optical properties (figs. S1–S3, table S2). For example, in one QD formulation, performing the shelling process for 5 hours resulted in an increase PL QY from 16.2% to 43.6% and a blue shift in the emission peak from 964 nm to 891 nm.

We then selected five QD formulations with emission peaks ranging from 828–891 nm to optimize in vivo light transmission and detection (Fig. 1G). These QDs were exposed to simulated solar light through pigmented cadaveric skin at seven-fold the intensity of the sun for a period that simulated five years of day/night exposure. One QD formulation, S10C5H, demonstrated significantly greater resistance to photobleaching than other formulations ($P < 0.05$), retaining 13 ± 3% of signal after five simulated years compared to the next best candidate, which retained only 4 ± 2% of its initial signal (Fig. 1H). This represented an approximately 50-fold improvement in resistance to photobleaching compared to the top-performing organic dyes tested. As a result, S10C5H was chosen for subsequent experiments. These QDs were 3.7 ± 0.6 nm in diameter and displayed the chalcopyrite phase structure characteristic of bulk $CuInSe_2$ (Fig. 1I, fig. S4).

Quantum dot encapsulation

Following synthesis, a subset of S10C5H QDs was encapsulated in poly(methyl methacrylate) (PMMA) microspheres using a spontaneous emulsion/solvent evaporation technique (Fig. 2, A–D). Emulsion parameters such as surfactant concentration and homogenization speed were refined to produce particles that contained 60% QDs by mass with an average size of 15.7 ± 5.3 μm (Fig. 2E). Encapsulated QDs displayed a similar but slightly red-shifted emission peak due to Förster resonance energy transfer in closely-packed QDs (Fig. 2F). Despite the about 40% loss of signal per mass due to the presence of PMMA, these particles still exhibited bright fluorescence (Fig. 2G), which was stable for months in phosphate buffered saline at 37°C (Fig. 2H). QDs embedded in PMMA also demonstrated consistent fluorescence intensity over a pH range that would be physiologically relevant in the phagolysosome (fig. S5).

Microneedle geometry optimization

To determine the optimal microneedle geometry for this application, finite element analysis was performed. 50 shapes ranging from a cone to a cylinder at a fixed height of 1500 μm were mechanically analyzed to ensure deep delivery of QDs into a permanent (non-shedding) layer of skin (figs. S6, S7). Important design criteria were to provide ample resistance to mechanical failure while also achieving a high deliverable volume, defined as the volume near the dissolving microneedle tip. Finite element analysis identified that microneedles with diameters of 100 or 200 μm were prone to failure due to both bending and axial loading, therefore all subsequent studies used needles 300 μm in diameter. Both the mechanical performance and deliverable volume from the needles were heavily

dependent on alpha (the proportion of microneedle height that was cylindrical) (Figs. 3, S6, S7). Increasing alpha generally contributed to higher deliverable drug volume, improved buckling resistance, and decreased maximum stress and displacement under axial loading while increasing maximum stress under bending. From these simulations, a value of 0.5 was selected for alpha. The maximum von Mises stress for our chosen microneedle geometry under bending and axial loading were 9.46 MPa and 8.71 MPa, respectively, the axial and bending displacement were found to be negligible, and the critical load factor was 0.0146 (fig. S6). After considering these factors along with deliverable volume, a microneedle with a 300 μm-wide cylindrical base that was 750 μm in height with an upper cone 750 μm in height was selected as a leading candidate for further study.

To verify in silico modeling data, we down-selected to three 3×3 arrays of microneedles: a 1500 μm cone (Fig. 3, A and B), a 750/750 μm cylinder/cone (Fig. 3, C and D), and 1250/250 μm cylinder/cone (Fig. 3, E and F) were printed using two-photon polymerization to create a master mold in photoresist. These shapes were maintained when the photoresist masters were used to produce inverse polydimethylsiloxane molds and ultimately positive dissolvable microneedles composed of poly(vinyl alcohol) and sucrose (Fig. 3G).

The force required to penetrate synthetic human skin or explanted pig skin with non-degradable in silico-optimized needles (750/750 μm cylinder/cone) was not significantly different from conical needles ($P = 0.46$ and $P = 0.07$, respectively), which have a lower deliverable volume, but substantially less force than the blunter (1250/250 μm cylinder/cone) needles was required (Fig. 3H). Decreasing the spacing of microneedles from 3.23 mm to 1.57 mm (1×1 cm and 0.5×0.5 cm patch sizes, respectively) did not affect the amount of force required for penetration (Fig. 3I). As a result, we confirmed our selection of microneedles with a height of 1500 μm, diameter of 300 μm, and alpha of 0.5 as the best combination of penetration depth, resistance to mechanical fracture, and maximum capacity for microparticle delivery.

Smartphone imaging system design and ex vivo skin penetration

To enable the imaging of NIR QDs in a field setting, we designed an inexpensive, smartphone-based imaging system. A 780 nm NIR light-emitting diode (LED) was paired with an 800 nm short-pass filter and aspheric condenser with diffuser to excite the QDs (Fig. 4A). For NIR fluorescence detection, a Nexus 5x smartphone (Google) was stripped of its stock short-pass NIR filter and paired with an 850 nm long-pass color glass filter and an 850 nm long-pass dielectric filter set in a poly(lactic acid) 3D printed phone case (Fig. 4B). Imaging a QD-loaded microneedle patch with and without the long-pass emission filters demonstrated the ability to filter background light while retaining NIR QD signal transmission (Fig. 4, C and D). All imaging was performed under ambient indoor lighting with no measures taken to reduce environmental background.

We then tested the ability of microneedles to deliver fluorescent microparticles into explanted tissue samples. A simple spring-loaded applicator was used to administer microneedles into ex vivo pig skin and human cadaveric skin for a duration of two minutes, in accordance with the optimal wear time identified by the global health organization PATH (19). Prior to application, microneedles appeared sharp with optically dark tips where QD-

loaded microparticles were embedded (Fig. 4, E and F). After application, microneedles were blunted as a result of the partial dissolution of the tip (Fig. 4, G and H). Although many fluorescent microparticles remained within the body of the needle, the transfer of QD-loaded particles from the 4×4 microneedle array into both pig skin (Fig. 4, I–L) and pigmented human skin (Fig. 4, M–P) was obvious when imaged using our NIR-adapted smartphone camera, yet not apparent by naked eye, as intended.

Pattern imaging, manual analysis, and machine learning-based pattern recognition

After confirming penetration and dissolution ex vivo, an eight-day study was performed to assess in vivo delivery. Microneedle patches containing QDs were administered to the rear flank of Wistar rats, as shown in movie S1. Prior to administration, hair at the application site was removed using an electric razor and depilatory cream. Microneedles were applied using a spring-loaded applicator and held in place for two minutes to allow for partial dissolution. This study revealed the importance of encapsulating QDs to ensure their delivery and prolonged residence in the body. Unencapsulated QDs resulted in very little and inconsistent transfer into the skin, likely due to their hydrophobicity (Fig. 5A). Alternatively, encapsulated QDs showed a much higher transfer of fluorescence into the skin that resulted in a NIR signal that was 10-fold higher than unencapsulated QDs (Fig. 5B). Over the days following administration, the signal from unencapsulated QDs was no longer apparent after 24 hours, whereas the signal from encapsulated QDs decreased on the first two days after application but then seemed to stabilize (Fig. 5C).

Next, to test the longevity of QD-containing PMMA microparticles in vivo, we administered patches containing eight microneedles in one of three distinct patterns: A circle on day 0, a cross on day 28, and a rectangle on day 56 and performed longitudinal imaging over nine months (Fig. 5, D–I). On the day of application, markings were visible on the skin for 100% of needles (120/120) with very high contrast. By the 24-week time point, 92% (110/120) remained visible with somewhat lower contrast than on the day of application. The number of marks per pattern at this time was 7.3 ± 0.8, which was largely independent of the spatial distribution of microneedles at the time of administration [7.4 ± 0.8, 7.2 ± 0.8, and 7.4 ± 0.8 for the circle, cross, and rectangle, respectively] (Fig. 5J). Fluorescent marks exhibited an average signal that was 29-fold, 23-fold, and 29-fold higher than background at 3, 6, and 9 months after administration, respectively, when considering the aggregate of all patterns (Fig. 5K). There were no statistical differences between the signal at 3 and 6 months ($P = 0.53$), 3 and 9 months ($P = 0.998$), or 6 and 9 months ($P = 0.50$).

Although patterns were easy to manually identify, we aimed to automate this process to improve its ease of implementation and thus potential clinical impact. To eliminate the need for personnel training and minimize opportunities for human error, we developed a machine learning algorithm based on the AlexNet neural network (20) to automatically classify each pattern (fig. S8). Using this neural network, we were able to correctly classify 100% of test image patterns (210 images total) that were collected biweekly for up to 30 weeks. In addition to correctly classifying all patterns, the probability of those classifications was also very high, with no trend towards lower probabilities over time (Fig. 5L). Of the 210 images analyzed, the lowest classifications probability for image was 98.4% for the cross pattern in

one rat on day 154. This data suggests that changes in signal intensity occur soon after administration (within three months), but that this does not affect detection reliability. This is also supported by qualitative images shown in Fig. 6 that depict dimmer signals between 0 and 12 weeks, but no further substantial losses between 12 and 24 weeks.

QD-loaded microparticle biocompatibility and co-delivery with polio vaccine

We then sought to test the in vitro and in vivo biocompatibility of our QDs. In vitro evaluation of cytotoxicity confirmed that our custom QDs composed of $CuInSe_2$ cores and ZnS:Al shells were less toxic to macrophages than commercially-available PbS QDs with a similar oleic acid surface treatment (Fig. 7A). Whereas no dose-dependent toxicity was observed in the range of S10C5H QD concentrations tested, we did observe a trend in PbS QD toxicity with a significant drop in cell viability at 1000 μg/ml ($P < 0.05$).

Histological examination of the local tissue response revealed tissue damage consistent with needle penetration one day after administration (Fig. 7, B and C). A minimal foreign body reaction was observed at two weeks (Fig. 7, D and E) and four weeks (Fig. 7, F and G). At both later time points, there appeared to be a small number of macrophages and foreign body giant cells at the site of administration. No fibrous encapsulation was observed over the time points collected, supporting the biocompatibility of the microparticles. In general, these results suggest that the PMMA-encapsulated S10C5H QDs largely remain local and are well-tolerated by the body. These observations were in agreement with visual observation of live animals over the days after microneedle administration, which showed no obvious signs of irritation beyond the date of application.

To observe the compatibility of this approach with vaccine delivery, we evaluated the immune response to three doses of microneedle-delivered Salk Inactivated Poliovirus Vaccine Type 2 (IPV2) administered at 0, 1, and 2 months with or without QD-loaded microparticles. IPV2 co-administered with microparticles induced total and neutralizing α-IPV2 antibody titers that were not statistically different ($P = 1.00$ and $P = 0.91$, respectively) from those achieved by IPV2 delivered by microneedles alone (Fig. 7, H and I). Total and neutralizing titers induced by microneedles containing QD-loaded microparticles and IPV2 were also non-inferior to three subcutaneous injections of IPV2 ($P = 0.25$ and $P = 0.32$, respectively) despite the use of a sub-optimal formulation, suggesting a strong dose-sparing effect since only 25 ± 2% of the vaccine retained its D-antigenicity during microneedle fabrication and a large fraction of IPV2 remained undelivered within the incompletely dissolved microneedles. Despite the substantially lower dose of antigen delivered in its immunity-conferring conformation, the neutralizing antibodies achieved were well above the threshold considered protective by the U.S. Centers for Disease Control and Prevention (21).

Discussion

To maximize the utility of this technology for vaccination campaigns, we aimed to create a platform compatible with microneedle-delivered vaccines that could reliably encode data on an individual for at least five years after administration. In addition, this system also needed to be highly biocompatible, deliver a sufficient amount of dye after an application time of two minutes or less, and be detectable using a minimally-adapted smartphone. Given the

limitations of organic dyes (water solubility) and inorganic dyes [rare earth metal toxicity (22), low fluorescence, processing difficulty], quantum dots were an attractive option as a potentially bright, photostable, and tunable alternative. However, clinical implementation of QDs has been stymied by the toxicity of their core elements, such as cadmium and lead (23). To overcome these safety concerns—which are especially important because these materials would be given to healthy children—we chose to synthesize custom QDs composed of more well-tolerated elements. We identified an optimal fluorescent emission range of 850–1100 nm. Operating in this range mitigates the potential cultural opposition to visible skin markings, reduces background from ambient light, minimizes light absorption by tissue at wavelengths below 850 nm (24), and maximizes signal detection by avoiding the poor sensitivity of inexpensive silicon-based detectors to light above 1100 nm (25). Although the use of fluorophores at the higher end of the NIR-II window (1000–1700 nm) would further improve tissue transparency and reduce background (26), appropriate detectors for these wavelengths (indium gallium arsenide) are typically considered cost-prohibitive (27), which could render this approach infeasible for widespread implementation.

Fluorophore photobleaching under accelerated solar light exposure enabled us to predict signal loss associated with sun exposure over long periods of time. As expected, organic fluorophores degraded relatively quickly despite protection by heavily pigmented skin, which absorbs a large fraction of ultraviolet (UV) and visible light. These dyes also exhibited strong self-quenching in the dry state and therefore had to be studied in a dispersed, hydrated state. This self-quenching property is problematic for this microneedle-delivered recording system because it limits the packing density of the dye, and thus its brightness. Alternatively, QDs performed very well under light exposure and have a larger Stokes shift, which enables them to avoid substantial reabsorption and therefore be used in a densely packed format.

Although the accelerated photobleaching assay does not perfectly mimic the real-world use case, it does provide evidence supporting the longevity of QDs compared to organic dyes. Further, this experimental setup may overestimate photobleaching because it assumes that skin is in direct sunlight every hour of the day that the sun is out. If administered at the thigh, where current vaccines are administered to infants, this area may be covered by clothing and/or in an area that is not exposed to direct sunlight for some portion of the daytime. In addition, photobleaching may also be enhanced in this experiment since seven-fold more intense light results in greater energy transfer per time, potentially enabling QD degradation to proceed more quickly.

PMMA was used as a non-degrading, encapsulating material for QDs to improve biocompatibility and enhance tissue permanence. The large size of microparticles (15.7 ± 5.3 μm) was also hypothesized to minimize clearance because previous studies have shown that larger particles are more resistant to clearance by macrophages, the most relevant cell type for clearing foreign material (28). The flexibility of QD surface coating also enabled us to make QDs soluble in the same organic solvent as PMMA, which helped dramatically enhance loading given that a traditional double emulsion technique (water-in-oil-in-water) cannot achieve 60% w/w.

We hypothesized that, unlike microneedle-delivered vaccines which must simply break the skin's water barrier to deliver their payload effectively (29), these fluorescent microparticles must be delivered below the shed layers of skin to ensure their long-term residence in tissue. Therefore, we aimed to create needles 1500 μm in length. To successfully penetrate to this depth, the microneedles must resist mechanical stress, deflection, and displacement upon insertion into skin. To effectively deliver PMMA-encapsulated QDs into the skin, the microneedles must pierce the skin without fracturing. The critical load factor of 0.014557 was higher than the values reported for carboxymethyl cellulose microneedles using the same simulation procedures (30). The final selection of alpha=0.5, height=1500 μm, and width=300 μm avoids critically low mechanical robustness against all the major mechanisms of mechanical failure. Using a larger diameter and larger alpha increased the volume of material and thereby the number of QD-loaded particles that are available for transfer into the skin. The drawback of this is the potential increase in pain and higher penetration force requirements. However, although pain perception has been shown to increase with the diameter of hypodermic needles (31–33), the amount of pain induced by our microneedle patch is likely less than for traditional needles, as has been shown elsewhere (34). Further, a previous study has shown that tip angle does not significantly impact pain upon needle insertion (35), so the effect of alpha (effective tip angle) on pain perception was not considered. These needles are slightly smaller in diameter than a 30-gauge needle and therefore should minimize both pain and the force required for skin penetration (36). Lastly, the lateral microneedle spacing results in a patch, and subsequently intradermal pattern, with a footprint of 0.25 cm^2. This spacing was sufficiently large to allow each needle to act independently and thereby allow force requirements to scale linearly with needle number (37).

Over the past decade, smartphones have become ubiquitous in many areas of the world, including the developing world despite limited infrastructure (38). Because these phones offer on-board processing power, camera applications, and inexpensive consumer-grade camera modules, we chose to adapt an existing smartphone to enable NIR imaging rather than build a completely new imaging system. In addition, we believe that familiarity with the function of these devices will lessen the learning curve to using the phone for NIR imaging in a field setting. Whereas a stock Nexus 5x camera is built with a short-pass filter to prevent NIR light from affecting images, we wanted the exact opposite—the elimination of light in the visible range and passage of NIR light. In addition, we needed the new filters to block reflected light from LED illumination. Therefore, after stripping the stock short-pass filter, we added a pair of 850 nm long-pass filters, which would block both environmental light and LED illumination. A dielectric filter was used to impose a sharp cut-off at 850 nm and paired with an 850 nm color glass filter to eliminate the passage of visible light entering the filter at a very small angle, which we observed to be problematic with the dielectric filter alone (39). These optics were fit into a 3D-printed phone case customized for SM1-threaded components (1.035”−40) to fit with commercially-available optical components.

Because both excitation and emission light can be absorbed by the body, we needed to create a system where both stages were within the optical imaging window. Although QDs are broadly excitable and exhibit higher quantum yield when exited at lower wavelengths (UV and visible light), high absorption from tissue components such as hemoglobin, water, and

melanin at these wavelengths greatly attenuates the signal. Given previous studies examining the relative absorption of these components, excitation at higher wavelengths was deemed worth the trade-off. For example, our leading candidate, S10C5H, exhibited a PL QY of 43.6 ± 0.1% upon excitation with a 405 nm laser and a PL QY of 31.3 ± 0.1% when excited with an 808 nm laser, but would be subjected to an increase in absorption from hemoglobin and melanin on the order of one log unit each (40). We chose to use a 780 nm LED rather than a laser because of the reduced cost, safety concerns, and maintenance combined with improved portability. Adapting a laser to this setup would have required a diffusor or beam splitter to spread the light, safety mechanisms, and potentially some type of cooling apparatus. These components would add cost, complexity, and size, which are undesirable for distributed mobile use. Alternatively, an LED offered low cost, inherently diffuse illumination, and safety/power advantages. The only consideration necessary to use an LED was the considerably wider emission profile (28 nm full width at half maximum); however, this was solved using a simple 800 nm short-pass filter to ensure a 50 nm gap between excitation light and light collected by the adapted smartphone.

NIR images collected with the smartphone at various ISO and shutter speed ratings were manually cropped to enable the comparison of NIR signal intensity over time. Manual ISO and shutter speeds were necessary to enable longitudinal comparison. The auto-exposure setting was not well-adapted for NIR imaging, as might be expected, and would often select higher exposure settings to make the field brighter to the point where the background was bright and the signal was highly saturated. Selection of the correct ISO for a pattern was critical for accurate analysis of both signal-to-noise ratio (SNR) as well as machine learning classification. To enable accurate SNR quantification, consistent imaging settings that produced non-saturated pixels at all time points were selected. In the future, custom auto-exposure settings could be implemented to automate this process.

The greatest reduction in user-identifiable signal occurred soon after administration, suggesting that some microneedles had not delivered QD-loaded microparticles to a sufficient depth—a phenomenon possibly exacerbated by the high elasticity of rodent skin (41). A portion of particles may have been deposited on the skin rather than in the skin and thereafter cleared by external perturbation. The QD signal stabilizes rather quickly and then presents a fairly consistent SNR at 3, 6, and 9 months, indicating that microparticle clearance likely primarily occurs at early time points (less than three months). This is further supported by the imaging of patterns in vivo at short time points which showed considerable loss in the days following application before stabilizing.

AlexNet was chosen for its classification accuracy, having been trained originally on more than 1 million images and having demonstrated ability to classify images into 1,000 categories (20). Despite relatively little training data (30 images per pattern), AlexNet classified images with high accuracy. Overall, 80 images were tested for the circular pattern, 70 for the cross pattern, and 60 for the rectangular pattern originating from five distinct pattern applications. The modified transfer-based convolutional neural network using AlexNet provided accurate detection confidence. Further, because there was no trend towards lower machine learning classification probability at three, six, and nine months, it appears that the patterns are stable after an acute period of signal loss, which is also

supported by short-term quantitative data and long-term qualitative data. Based on optical images of microneedles before and after administration, in vivo NIR imaging, and projections for photobleaching from in vitro experiment, we estimate that <1 μg of particles (<600 ng of QDs) is required to retain a detectable signal for five years.

Regarding accuracy, machine learning algorithms for image classification match and typically exceed manual inspection (42,43). Whereas the human eye is ill-equipped to distinguish low grayscale value differences in images that are dim or have poor contrast (grayscale values of 1 vs 10), AlexNet's ability to use quantitative rather than qualitative information seems to make this distinction trivial. This effect is readily apparent when the grayscale photo values are represented as a rainbow heat. AlexNet was particularly valuable when markings were missing, dim, or imaged at an unusual angle. Given the minimal training data used, it was important that images were collected using settings that roughly approximated the range of brightness/signal spread of images used for training. More training data and/or consistent auto-exposure would mitigate this potential issue long-term. Similarly, more patterns could be incorporated into the model to expand the variety of data that can be encoded. In the real world use case, this automated classification will eliminate classification subjectivity that could interfere with the accuracy of this approach. Synthetic data could also be produced using image augmentation to train the algorithm without the need for actual patch applications. However, the accuracy of this method could be lower if the variability in application exhibited in the synthetic data did not replicate the features of real microneedle patch applications in the test data. In our experience, training AlexNet with 5,000 synthetic images yielded a real-world data classification accuracy of 92% for the circle and 97% for both the cross and rectangle. Future training data could also include a fourth classification category for all images that do not closely resemble any of the patterns. This would be essential for real-world use when the presence of a pattern is uncertain.

For this encoding system to be clinically useful, microneedles and NIR microparticles must be biocompatible and, if applicable, maintain the utility of any co-delivered vaccines. Histology showed that the particles were well-tolerated in the body, similar to largely inert PMMA-based tattoo dyes (44), although some macrophages were observed. The accumulation of macrophages observed around the particles was less than other studies have shown for poly(lactic-co-glycolic acid) microparticles (45), for example, which are present in many FDA-approved drug delivery systems (46). In addition, histological images demonstrated that microneedle-delivered particles were delivered to a depth similar to professional tattoos (47), which supports their potential for long-term NIR detection.

In addition to the stand-alone value of an intradermal information encoding and detection platform, this system may offer greater advantages when co-delivered with vaccines. By delivering both agents in the same microneedle patch, there is the potential to realize production cost advantages and eliminate the possibility of misuse (applying the encoding patch without the vaccine). However, to function in combination with microneedle vaccines currently under development, PMMA-encapsulated NIR QDs must not interfere with the robust immune response generated by intradermal antigen delivery. To ensure sufficient QD delivery and vaccine stability after fabrication (a process that includes multiple days under high vacuum), the amount of sucrose in the microneedle formulation and application time

were both increased. Despite these modifications, a decrease in vaccine stability (IPV2 D-to-C conversion) was still observed and a considerable microneedle volume was not transferred to the skin during application, which would be expected to reduce the magnitude of the immune response. Nevertheless, microneedle-treated groups yielded total and neutralizing antibody titers against IPV2 that were similar with theoretical dose-matched subcutaneous injections and were above the threshold known to confer protection in humans, regardless of the presence of encapsulated QDs. This was observed despite substantial losses during formulation and administration, and is likely due to the dose-sparing effects of intradermal delivery (16,17). Although the addition of polymer could have had an adjuvant effect, this was not observed, likely because of the well-tolerated, largely inert nature of our PMMA microparticles, as demonstrated in our histological data. These results support the clinical potential for using these microneedles to co-administer an invisible marking agent and a vaccine in one application.

This study supports the long-lived, reliable pattern detection of QDs; however, like many preclinical studies, it is limited in duration and relies on small animal models. We present data characterizing signal expression over 9 months in animals and in vitro accelerated solar light photobleaching studies which suggest that detectable markings would persist to the target time point of five years. Based on histology and longitudinal imaging studies we would not anticipate a substantial decrease in signal within five years after application, however we did not explicitly demonstrate this due to time constraints which exceed the typical life span of our animal model.

In summary, we have demonstrated proof-of-concept for a platform capable of invisibly recording data in the skin. To establish this system, we synthesized, encapsulated, and delivered cadmium- and lead-free photostable QDs into the skin using a custom microneedle array, adapted a smartphone to create an inexpensive NIR imaging system, and demonstrated the ability to accurately detect patterns in vivo for a period of 9 months using a semi-automated machine learning algorithm. Transferring this technology to the clinic will require several additional steps including preclinical safety and toxicology studies, manufacturing scale-up, and first-in-human studies. Additional in vivo small animal studies will aid in the robust characterization of local and systemic responses to QD-loaded PMMA microparticles and microneedle patches to ensure quality, safety, and reliability. Formative studies in which users test the devices, including the packaging and labeling, will need to be conducted to improve components for commercialization and to manufacture devices for testing in human studies. Ultimately, we believe that this invisible, “on-body” technology opens up new avenues for decentralized data storage and biosensing applications that could influence the way medical care is provided, especially in the developing world.

Materials and Methods

Study design

These studies were designed to evaluate the suitability of intradermal near-infrared fluorescent microparticles as a reliable, long-term detection method. To evaluate this technology under typical field conditions, we used an adapted smartphone in ambient light to determine success criteria, except in circumstances where spectral and/or highly

quantitative data was necessary to characterize our materials. In vivo studies were generally preferred to assess the performance of our delivery and detection systems and animals were randomly assigned to different experimental groups at the onset of each study. The use of machine learning for detection eliminated the need for blinding. In vitro studies were performed with three replicates and in vivo studies with five replicates, unless otherwise noted.

Quantum dot synthesis

Stoichiometric copper indium selenide ($CuInSe_2$) cores were synthesized by mixing 1.5 mmol copper(I) iodide and 1.5 mmol indium(III) acetate in 1.5 mL of 1-dodecanethiol and 45 mL of 1-octadecene (ODE) based on a modified procedure (48). The reaction mixture was then degassed under vacuum for 20 min, purged with nitrogen for 20 min, and degassed for an additional 45 min at 120°C. Next, 1.5 mL of oleic acid was added into the mixture and the solution was degassed for 20 min. After another 20-min nitrogen purge, the solution was heated to 175°C before the injection of selenium stock solution. A selenium stock solution was first prepared by mixing 3 mmol of selenium powder and 3 mL of oleylamine (OLA) in 3 mL of 1-dodecanethiol (49). The selenium solution was degassed under vacuum for at least 30 min at 60°C before injected into the reaction mixture. The reaction mixture was heated to 200°C and maintained at this temperature for 30 min under the protection of nitrogen.

ZnS:Al shells were formed around $CuInSe_2$ cores through the dropwise addition of a stock solution containing zinc and aluminum. The zinc precursor of the stock solution was prepared by mixing 30 mmol of zinc acetate in 30 mL of OLA and 30 mL of ODE, degassing for 20 min, and purging with nitrogen for 20 min. Next, the solution was heated to 120°C and degassed under vacuum. The Al precursor mixture consisting of 9 mmol of $Al(IPA)_3$, 5.4 mL of 1-dodecanethiol, and 36 mL of ODE was degassed for 20 min and purged with nitrogen for 20 min. The vessel was then sealed and sonicated for 1 h at 60°C (50). The aluminum stock solution was then added to the zinc stock solution using a glass syringe and long needle. After mixing the zinc and aluminum precursors, the resulting shell stock solution and 1-dodecanethiol (DDT) was added dropwise to the reaction mixture of $CuInSe_2$ cores at 0.1 mL/min using a gas-tight 25 mL syringe. At the same time, 15 mL of DDT was added at a rate of 0.5 mL/min to thermally trigger the release of sulfur (51). The reaction was allowed to proceed for varying amounts of time, depending on the formulation. Afterward, the reaction solution was cooled to room temperature and precipitated twice into acetone, once into a 50:50 solution of acetone and methanol, and twice more into methanol. Between each round of precipitation, QDs were resuspended in a minimal amount of toluene and oleic acid that was added dropwise until the solution turned transparent. After the final precipitation step, QDs were dispersed in toluene.

Photobleaching analysis

Organic dyes required different imaging conditions than inorganic dyes and QDs because of their small Stokes shift and therefore high propensity to self-quench in the dry state. Organic fluorophores were dissolved in water at a concentration of 10 μg/mL, which was found to be within the linear absorbance range for all dyes. 50 μL of each dye was added to a black-

walled 384-well plate, covered with a 1 mm-thick quartz slide, and sealed with parafilm at the edges to prevent evaporation during light exposure. The plate was then read using a Tecan Infinite M200 Spectrophotometer Alexa Fluor 790 (784/814 nm ex/em), DyLight 800 (760/810 nm ex/em), IRDye 800CW (768/798 nm ex/em), IR-820 (710/820 nm ex/em), Sulfo-Cyanine7 (750/773 nm ex/em), VivoTag 800 (785/815 nm ex/em), and indocyanine green (805/835 nm ex/em).

Samples were then placed under a 300W PV Cell Testing Solar Simulator Model 16S-300–002 (Solar Light). The ozone-free short arc xenon lamp was used filtered using an air mass 1.5 filter and focusing lens to expose samples to conditions mimicking the spectral distribution and power density of sunlight at 7-fold the intensity of the sun (695 mW/cm^2). A 2 mm-thick piece of pigmented human cadaver skin from donors age 21–68 years who self-identified as African American was overlaid onto the sample to recapitulate light absorption by tissue above an intradermal fluorophore. Skin was kept hydrated by a continuous flow of water over the surface and chilled from below using a CP-200HT-TT Peltier-Thermoelectric Cold Plate Cooler (TE Technology) to prevent damage to the skin. Samples were periodically removed from the solar simulator and imaged using the spectrophotometer. This experiment was repeated three times with one replicate each.

Inorganic dyes and QDs were capable of being imaged in their dry state, so a modified protocol was used. Holes were punched in a black silicone sheet using a 2 mm stainless steel biopsy punch to create space for dyes. The silicone sheet was then treated with air plasma for 1 min on high power at 500 mTorr. The sheet was then placed on a 2.54 × 2.54 cm quartz slide, which allowed it to adhere in a water-tight manner. Suspensions of IRCD2 and IRDC3 at 10 mg/mL in water were deposited 2 μl at a time and allowed to dry until a total of 10 μl had been deposited. The same steps was performed for ZnS:Al-coated $CuInSe_2$ QD solutions at 10 mg/mL in toluene. Double-sided tape and parafilm were then used to seal a glass slide to the other side of the black silicone. The sample was then placed quartz slide-up beneath a piece of pigmented cadaveric skin in a metal block under continuous hydration on a cold plate cooler and exposed to light at 7-fold solar intensity. At predetermined time points, samples were removed from light and imaged using a custom NIR-imaging platform consisting of a 500 mW laser emitting at 808 nm and TE-cooled mount powered by a LDC210C Laser Diode Controller and TED200C Temperature Controller, a 15x achromatic Galilean beam expander, protected silver mirror, 850 nm color glass long-pass emission filter, and a high-sensitivity USB 3.0 CMOS Camera (DCC3240N) affixed to an optical breadboard (Thor Labs) inside a dark work enclosure (U.S. Laser). Images were collected at different exposure lengths for different dyes ranging from 10 to 2000 ms. The longest exposure length that did not saturate the 10-bit pixel depth was used for each dye at all time points. Owing to the length of this experiment, all samples (n=3) were run simultaneously. For all photobleaching experiments, skin was replaced every 2–4 days to reduce the effects of melanin degradation. Intensity data was quantified using ImageJ (National Institutes of Health) and normalized by selecting a region of interest (ROI) around a well and comparing the intensity above background in that image to the intensity above background of the corresponding ROI at the beginning of the experiment (52). All photobleaching data is reported as simulated days of exposure based on a 12-hour light/dark cycle.

Quantum dot encapsulation

QD-loaded PMMA microparticles were formed using an oil-in-water emulsion/solvent evaporation technique. Briefly, 150 mg of oleic acid-functionalized QDs and 100 mg of PMMA were dissolved in 2 mL of dichloromethane. This solution was then added to 50 mL of 1% PVA (88% hydrolyzed, M_w 31,000) solution in water. The resulting solution was emulsified at 5,000 RPM for 1 min using a T 18 digital ULTRA-TURRAX homogenizer (IKA Works) and subsequently stirred at 250 RPM for 3 hours to allow solvent to evaporate. Particles were the centrifuged at 1,000 RCF after which the supernatant was removed. Particles were then washed four times by adding deionized water, centrifugation at 1,000 RCF, and supernatant removal. The resulting particles were resuspended in deionized water and measured using a Multisizer 3 (Beckman Coulter) with a 100 μm aperture. Data was smoothed using an eleven-frame moving window and plotted as a histogram with 300 equal-sized bins ranging from 2.1 to 59.9 μm. QD-loaded microparticles were then imaged using optical microscopy and scanning electron microscopy (SEM) to observe their shape. Optical imaging was performed using an Olympus MX40 Inspection Microscope with a ToupCam Industrial Digital Camera (ToupTek Photonics). In preparation for SEM, samples were deposited on double-sided carbon tape and coated with a thin layer of Au/Pd using a Hummer 6.2 Sputtering System (Anatech) to prevent charging. Imaging was then performed using a JEOL JSM-5600LV scanning electron microscope with an acceleration voltage of 5 kV.

The pH stability of S10C5H QDs in PMMA was determined by casting a solution onto the bottom of a plate to prevent agitation upon addition of the buffer. 150 mg of QDs and 100 mg of PMMA were added to 2 mL of DCM and sonicated for 5 mins. Using a glass pipette, about 5 μL of the QD solution was added to the bottom of a 96-well black walled glass bottom plate and dried overnight. 200 μL of PBS was then added to each well and the samples were incubated at 37°C for 24 hours. At this stage the initial intensity of the QD-PMMA samples were analyzed using a custom NIR-imaging platform as described above. To investigate the effect of pH on the intensity of the quantum dots, the PBS was replaced by a buffer solution at pH 4, 5, 6, 7.4 (PBS), or 10. The plate was then sealed to minimize solvent loss and incubated at 37°C. After 1, 4, and 22 hours, samples were removed from the incubator and QD intensity was measured using the custom NIR-imaging system with a 40 ms collection time. Intensity data was quantified in ImageJ and normalized by selecting an ROI around a well and comparing the intensity above background in that image to the intensity above background of the corresponding ROI at the beginning of the experiment.

Dissolvable microneedle fabrication and characterization

Water-soluble microneedle patches containing QD-loaded microparticles at the needle tips were fabricated using a solvent casting process. First, microparticles were resuspended in water, pipetted onto the top of the PDMS mold (4 μL/microneedle), and centrifuged at 3,234 RCF for 5 min. Excess solution was cleared from the top of the mold and the solution was allowed to dry leaving behind particles in the tips of the mold. This process was repeated when loading was lower than desired or unevenly distributed. Approximately 300 μL of a 17% w/v sucrose and 17% w/v PVA solution in water was then dispensed on top of the mold and centrifuged at 3,234 RCF for 5 min. Molds were then left at room temperature in a

laminar flow hood as an initial drying stage. Laser-cut acrylic discs were then affixed to double-sided tape and attached to the back side of the solidified microneedle patch. The patch was then carefully removed from the mold and stored for an additional 72 hours under vacuum desiccation.

Smartphone modifications

A smartphone camera was adapted with commercially-available optical components purchased from Thorlabs to enhance NIR quantum dot detection in the NIR. To enable NIR detection, the stock short-pass IR filter was removed from a Google Nexus 5 smartphone. A smartphone case was then designed and 3D printed to interface tightly with optical components possessing SM1 threading directly in front of the rear-facing camera. An 850 nm long-pass dielectric filter (FEL0850) and 850 nm long-pass colored glass filter (FGL850) were placed in parallel in a lens tube attached to the smartphone case and held in place with a retaining ring. For QD illumination, a 780 nm, 200 mW mounted LED (M780L3) powered by a T-cube LED Driver (LEDD1B) and 15 V, 2.4 A power supply (KPS101) was used. In order to augment the shape and spectrum of emission, an 800 nm dielectric short-pass filter (FEL0800) and aspheric condenser lens with diffuser (ACL2520U-DG6-B) were used in an adjustable lens tube. All imaging was performed using the Camera FV-5 Lite app (FGAE Studios).

Biocompatibility of encapsulated quantum dots

Microneedles containing encapsulated QDs were administered to Wistar rats (Charles River) 8–12 weeks of age weighing approximately 250 g to assess in vivo biocompatibility. Rats were anesthetized via continuous inhalation of 2.5% isoflurane throughout the administration and imaging process. Hair removal was performed prior to microneedle administration by shaving the rear flank with an electric razor and applying depilatory cream for about 2 min. The area was then rinsed to remove excess hair, sterilized using an ethanol swab, and allowed to dry. Microneedles were applied using an MPatch Mini spring-loaded applicator (Micropoint Technologies) for 2 min. Rats were returned to their cages and housed until terminal time points at 1 day, 2 weeks, and 4 weeks (n = 4 per time point). At the time of sacrifice, rats were euthanized via CO_2 asphyxiation. Skin was explanted and fixed in formalin free tissue fixative (Sigma-Aldrich) for 24–72 hours. The relevant portion of the tissue was identified using the adapted smartphone, transferred to 70% ethanol, and embedded in paraffin wax. Samples were sectioned and stained with hematoxylin and eosin or Masson’s trichrome. Interpretation of the foreign body reaction was performed under the guidance of an experienced veterinary pathologist.

Longitudinal in vivo imaging of NIR patterns

Two longitudinal imaging experiments were performed to assess the short-term loss of signal after administration and long-term residence of microneedle-delivered particles. In both cases, QDs were administered to rats using dissolvable microneedle patches as described above and imaged periodically to observe signal intensity over time. At each time point, rats were anesthetized under continuous inhalation of 2.5% isoflurane and imaged with the 780 nm LED and NIR-adapted smartphone, maintaining a consistent imaging distance.

In the first experiment, microneedles containing PMMA-encapsulated and free (unencapsulated) ZnS:Al-coated $CuInSe_2$ QDs were compared to evaluate the potential benefits of encapsulation on initial signal intensity and signal retention. Encapsulated QDs were embedded in dissolvable microneedles using the protocol detailed above. Unencapsulated QDs were not readily dispersible in water, so the loading procedure was slightly modified. Prior to loading, PDMS molds were treated with air plasma using a Harrick Plasma Cleaner PDC-091-HP on high power at 500 mTorr for 1 min. QDs in toluene (4 μL per microneedle) were then deposited into the microneedle molds and centrifuged at 3,234 RCF for 5 min. Toluene was then allowed to dry. A solution of sucrose and PVA was then applied to the molds and centrifuged into the needles and allowed to dry using the fabrication steps outlined above.

After applying 16-microneedle patches, the highest non-saturating imaging settings were identified and used at all subsequent time points for that group. For the unencapsulated group, these settings were ISO 100 with a shutter speed of 1/30 sec. For the encapsulated group, these settings were ISO 100 with a shutter speed of 1/30 or 1/200 sec. For each animal and time point, approximately 20 images were collected with slightly different aim of the LED, which was controlled independently from the camera that remained in a fixed location. An ImageJ macro was then used to split images into their three constituent red, green, and blue channels, save the red channel in grayscale format, and identify the images with the maximum intensity. This image with the best aim was then used for subsequent quantification of signal-above background. Briefly, 80-pixel circular ROIs were applied to each of the 16 dots in the 4×4 array to quantify the average signal. The average grayscale intensity of the remaining pixels was subtracted to generate longitudinally comparable values for signal-above-background.

Based on this short-term study, a second long-term study was performed using encapsulated QDs in 8-needle microneedle patterns (circle, cross, or a rectangle) for image detection and machine learning analysis. Arrays were administered at 0 (circle), 4 (cross), and 8 (rectangle) weeks to mimic a common vaccination schedule in the developing world. A separate group was started in parallel to generate an image data set for training the machine learning algorithm. Images were collected every two weeks at a variety of ISO and shutter speeds, processed, and used for both SNR analysis and machine learning classification.

Microneedle-based vaccine delivery

The solution used to cast microneedles was altered in favor of additional sucrose (2:1 w/w sucrose:PVA) to potentially improve vaccine stability during processing. A solution of 34% w/v sucrose and 17% w/v PVA solution containing 3.2 DU of Salk type 2 inactivated poliovirus (IPV2, MEF-1 strain, Statens Serum Institut) was centrifuged into PDMS microneedle molds using the procedures detailed above. After processing, some microneedle patches were collected, resuspended in assay buffer, and evaluated using a D antigen-specific monoclonal sandwich ELISA for IPV2 to determine the amount of the vaccine still in its immunity-conferring state. A monoclonal antibody against IPV2 poliovirus (HYB 294-06-02, Thermo Fisher) was used as both the capture and detection antibody, which was made possible because of the multiple identical binding sites on IPV. To avoid species cross-

reactivity, a Lightning-Link Horseradish Peroxidase Kit (Novus Biologicals) was used to pre-bind the detection epitope. Briefly, 100 μl of antibody diluted 1:1500 in carbonate buffer (pH 9.6) was added to each well of a Nunc Maxisorp LockWell 96-well plate and incubated overnight at 4°C on an orbital shaker. Plates were then washed with phosphate buffered saline containing 0.05% Tween 20 three times and incubated in 300 μl blocking buffer containing the wash buffer and 5% w/v nonfat milk for 1 h at 37°C. Plates were again washed, and then loaded with 50 μl of samples. After 2 h incubation at 37°C, plates were washed 5 times and the Lightning Link-modified antibody was added at 1:833 in PBS. After 1 h incubation, plates were washed another 5 times and then 100 μl of a SIGMAFAST OPD substrate (Sigma-Aldrich) was added after resuspension according to the manufacturer's protocol. Following a color change, 150 μl of M sulfuric acid was added to each well to stop the reaction and absorbance values were read at 490 nm with a background reference of 630 nm using a spectrophotometer.

Microneedle patches not used for ELISA were applied to rats for a duration of 5 min using the protocol described above. After application, the portion of the microneedles remaining on the patch was collected, resuspended in assay buffer, and measured via the IPV2 D-antigen ELISA. A control group of rats received a dose-matched subcutaneous injection in the rear flank. These procedures were repeated 4 and 8 weeks later to provide rats with second and third doses. Rats were bled vial tail vein every two weeks following administration to collect serum for immunological analysis. Blood was collected in BD SST tubes (Product #365967, Becton Dickinson) and used according to the manufacturer's protocol to obtain serum, which was subsequently stored at −20°C until use. A total anti-IPV2 antibody ELISA was performed in house using an indirect ELISA, as previously described (53). IPV2 neutralizing antibody titers were determined by the U.S. Centers for Disease Control and Prevention using a protocol previously published (21).

Statistical analysis

Statistics were performed in GraphPad Prism using Student's t-test for pairwise comparisons and one-way ANOVA with Tukey's multiple comparisons test for comparing multiple groups at a significance level of $\alpha = 0.05$. In vitro toxicity experiments evaluating both QD type and concentration was analyzed using two-way ANOVA at a significance level of $\alpha = 0.05$. All in vitro experiments were performed in experimental triplicate unless otherwise noted. All in vivo experiments were performed with five experimental replicates unless otherwise noted. Data are reported in the text as mean ± standard deviation.

Supplementary Material

Refer to Web version on PubMed Central for supplementary material.

Acknowledgments:

We acknowledge W. H. Gates, D. Hartman, S. Hershenson, S. Kern, B. Nikolic, K. Owen, L. Shackelton, C. Karp, and D. Robinson for their guidance, R. T. Bronson for his pathology expertise, and the MIT Department of Comparative Medicine for their advice. We thank Dr. W. Weldon and his laboratory at the U.S. Centers for Disease Control and Prevention for performing neutralizing antibody titer studies, the Koch Institute Swanson Biotechnology Center for technical support, specifically the Hope Babette Tang (1983) Histology Facility and the

Peterson (1957) Nanotechnology Materials Core Facility as well as the Harvard University Center for Nanoscale Systems, and W.M. Keck Microscopy Facility at the Whitehead Institute.

Funding: This work was funded by the Bill & Melinda Gates Foundation grant OPP 1150646. Fellowship support for K.J.M. was provided by an NIH Ruth L. Kirschstein National Research Service Award (F32EB022416). L.J. thanks the Youth Innovation Promotion Association CAS (2018042), National Natural Science Foundation of China (81671755), and China Scholarship Council (201604910444) for financial support. This work was supported in part by the Koch Institute Support (core) Grant P30-CA14051 from the National Cancer Institute. This work was performed in part at the Harvard University Center for Nanoscale Systems (CNS), a member of the National Nanotechnology Coordinated Infrastructure Network (NNCI), which is supported by the National Science Foundation under NSF award no. 1541959.

References and Notes:

1. Legesse E, Dechasa W. An assessment of child immunization coverage and its determinants in Sinana District, Southeast Ethiopia. BMC Pediatr 15, 31 (2015). [PubMed: 25886255]
2. Black RE, Cousens S, Johnson HL, Lawn JE Rudan I, Bassani DG, Jha P, Campbell H, Walker CF, Cibulskis R, Eisele T, Liu L, Mathers C, Child Health Epidemiology Reference Group of WHO and UNICEF, Global, regional, and national causes of child mortality in 2008: a systematic analysis. Lancet 375, 1969–1987 (2010). [PubMed: 20466419]
3. Szilagyi PG, Rodewald LE, Missed opportunities for immunizations: a review of the evidence. J Public Health Manag Pract 2, 18–25 (1996). [PubMed: 10186652]
4. Pirkle CM, Dumontn A, Zunzunegui MV, Medical recordkeeping, essential but overlooked aspect of quality of care in resource-limited settings. Int J Qual Health Care 24, 564–567 (2012). [PubMed: 22798693]
5. Fields VS, Safi H, Waters C, Dillaha J, Capelle L, Riklon S, Wheeler JG, Haselow DT, Mumps in a highly vaccinated Marshallese community in Arkansas, USA: an outbreak report. Lancet Infect Dis 19, 185–192 (2019). [PubMed: 30635255]
6. Westphal DW, Eastwood A, Levy A, Davies J, Huppatz C, Gilles M, Lyttle H, Williams SA, Dowse GK, A protracted mumps outbreak in Western Australia despite high vaccine coverage: a population-based surveillance study. Lancet Infect Dis 19, 177–184 (2019). [PubMed: 30558994]
7. Lo Vecchio A, Cambriglia MD, Fedele MC, Basile FW, Chiatto F, Miraglia Del Giudice M, Guarino A, Determinants of low measles vaccination coverage in children living in an endemic area. Eur J Pediatr 178, 243–251 (2019). [PubMed: 30430239]
8. Miles M, Ryman TK, Dietz V, Zell E, Luman ET, Validity of vaccination cards and parental recall to estimate vaccination coverage: A systematic review of the literature. Vaccine 31, 1560–1568 (2013). [PubMed: 23196207]
9. Tao WJ, Petzold M, Forsberg BC, Routine vaccination coverage in low- and middle-income countries: further arguments for accelerating support to child vaccination services. Global Health Action 6, 1–8 (2013).
10. Valadez JJ, Weld LH Maternal recall error of child vaccination status in a developing nation. Am J Public Health 82, 120–122 (1992). [PubMed: 1536315]
11. Ogbuanu IU, Li AJ, Anya BM, Tamadji M, Chirwa G, Chiwaya KW, Djalal ME, Cheikh D, Machekanyanga Z, Okeibunor J, Sanderson C, Mihigo R, Can vaccination coverage be improved by reducing missed opportunities for vaccination? Findings from assessments in Chad and Malawi using the new WHO methodology. Plos One 14 (2019).
12. Katib A, Rao D, Rao P, Williams K, Grant J, A prototype of a novel cell phone application for tracking the vaccination coverage of children in rural communities. Comput Methods Programs Biomed 122, 215–228 (2015). [PubMed: 26363678]
13. Jain AK, Arora SS, Best-Rowden L, Cao K, Sudhish PS, Bhatnagar A, Koda Y, Giving Infants an Identity: Fingerprint Sensing and Recognition. Proceedings of the Eighth International Conference on Information and Communication Technologies and Development (Ictd 2016) (2016).
14. Nagar R, Venkat P, Stone LD, Engel KA, Sadda P, Shahnawaz M, A cluster randomized trial to determine the effectiveness of a novel, digital pendant and voice reminder platform on increasing infant immunization adherence in rural Udaipur, India. Vaccine 36, 6567–6577 (2018). [PubMed: 29162321]

15. Rouphael NG, Paine M, Mosley R, Henry S, McAllister DV, Kalluri H, Pewin W, Frew PM, Yu T, Thornburg NJ, Kabbani S, Lai L, Vassilieva EV, Skountzou I, Compans RW, Mulligan MJ, Prausnitz MR, TIV-MNP 2015 Study Group, The safety, immunogenicity, and acceptability of inactivated influenza vaccine delivered by microneedle patch (TIV-MNP 2015): randomised, partly blinded, placebo-controlled, phase 1 trial. Lancet 390, 649–658 (2017). [PubMed: 28666680]
16. Prausnitz MR Engineering Microneedle Patches for Vaccination and Drug Delivery to Skin. Annu Rev Chem Biomol 8, 177–200 (2017).
17. He YP, Hong C, Li J, Howard MT, Li Y, Turvey ME, Uppu DSSM, Martin JR, Zhang K, Irvine DJ, Hammond PT, Synthetic Charge-Invertible Polymer for Rapid and Complete Implantation of Layer-by-Layer Microneedle Drug Films for Enhanced Transdermal Vaccination. Acs Nano 12, 10272–10280 (2018). [PubMed: 30272942]
18. Vassilieva EV, Kalluri H, McAllister D, Taherbhai MT, Esser ES, Pewin WP, Pulit-Penaloza JA, Prausnitz MR, Compans RW, Skountzou I, Improved immunogenicity of individual influenza vaccine components delivered with a novel dissolving microneedle patch stable at room temperature. Drug Deliv Transl Re 5, 360–371 (2015).
19. Zehrung D, Jarrahian C, Giersing B, Kristensen D, Exploring new packaging and delivery options for the immunization supply chain. Vaccine 35, 2265–2271.
20. Krizhevsky A, Sutskever I, Hinton GE, ImageNet Classification with Deep Convolutional Neural Networks. Commun Acm 60, 84–90 (2017).
21. Weldon WC, Oberste MS, Pallansch MA, Standardized Methods for Detection of Poliovirus Antibodies. Methods Mol Biol 1387, 145–176 (2016). [PubMed: 26983734]
22. Rim KT, Koo KH, Park JS, Toxicological evaluations of rare earths and their health impacts to workers: a literature review. Saf Health Work 4, 12–26 (2013). [PubMed: 23516020]
23. McHugh KJ, Jing L, Behrens AM, Jayawardena S, Tang W, Gao M, Langer R, Jaklenec A, Biocompatible Semiconductor Quantum Dots as Cancer Imaging Agents. Adv Mater 30 (2018).
24. Hamblin MR, Demidova TN, Mechanisms of low level light therapy. Proc Spie 6140 (2006).
25. Smith AM, Mancini MC, Nie SM, Bioimaging second window for in vivo imaging. Nat Nanotechnol 4, 710–711 (2009). [PubMed: 19898521]
26. Antaris AL, Chen H, Cheng K, Sun Y, Hong G, Qu C, Diao S, Deng Z, Hu X, Zhang B, Zhang X, Yaghi OK, Alamparambil ZR, Hong X, Cheng Z, Dai H, A small-molecule dye for NIR-II imaging. Nat Mater 15, 235–242 (2016). [PubMed: 26595119]
27. Wilson RH, Nadeau KP, Jaworski FB, Tromberg BJ, Durkin AJ, Review of short-wave infrared spectroscopy and imaging methods for biological tissue characterization. J Biomed Opt 20 (2015).
28. Baranska A, Shawket A, Jouve M, Baratin M, Malosse C, Voluzan O, Vu Manh TP, Fiore F, Bajenoff M, Benaroch P, Dalod M, Malissen M, Henri S, Malissen B, Unveiling skin macrophage dynamics explains both tattoo persistence and strenuous removal. J Exp Med 215, 1115–1133 (2018). [PubMed: 29511065]
29. Matsuo K, Yokota Y, Zhai Y, Quan YS, Kamiyama F, Mukai Y, Okada N, Nakagwa S, A low-invasive and effective transcutaneous immunization system using a novel dissolving microneedle array for soluble and particulate antigens. J Control Release 161, 10–17 (2012). [PubMed: 22306332]
30. Loizidou EZ, Williams NA, Barrow DA, Eaton MJ, McCrory J, Evans SL, Allender CJ, Structural characterisation and transdermal delivery studies on sugar microneedles: Experimental and finite element modelling analyses. Eur J Pharm Biopharm 89, 224–231 (2015). [PubMed: 25481031]
31. Alam M, Geisler A, Sadhwani D, Goyal A, Poon E, Nodzenski M, Schaeffer MR, Tung R, Minkis K, Effect of Needle Size on Pain Perception in Patients Treated With Botulinum Toxin Type A Injections A Randomized Clinical Trial. Jama Dermatol 151, 1194–1199 (2015). [PubMed: 26352252]
32. Gill HS, Prausnitz MR Does needle size matter? J Diabetes Sci Technol 1, 725–729 (2007). [PubMed: 19885141]
33. Arendt-Nielsen L, Egekvist H, Bjerring P, Pain following controlled cutaneous insertion of needles with different diameters. Somatosens Mot Res 23, 37–43 (2006). [PubMed: 16846958]
34. Gill HS, Denson DD, Burris BA, Prausnitz MR, Effect of microneedle design on pain in human subjects. Clin J Pain 24, 585–594 (2010).

35. Praestmark KA, Jensen ML, Madsen NB, Kildegaard J, Stallknecht BM, Pen needle design influences ease of insertion, pain, and skin trauma in subjects with type 2 diabetes. BMJ Open Diabetes Res Care 4, e000266 (2016).
36. Masid ML, Ocana RH, Gil MJ, Ramos MC, Roig ME, Carreno MR, Morales JC, Carrasco ML, Hidalgo LM, Felices AM, Castano AH, Romero PC, Martinez PF, Sanchez-De la Rosa R, A patient care program for adjusting the autoinjector needle depth according to subcutaneous tissue thickness in patients with multiple sclerosis receiving subcutaneous injections of glatiramer acetate. J Neurosci Nurs 47, E22–30 (2015). [PubMed: 25225835]
37. Olatunji O, Das DB, Garland MJ, Belaid L, Donnelly RF, Influence of array interspacing on the force required for successful microneedle skin penetration: theoretical and practical approaches. J Pharm Sci 102, 1209–1221 (2013). [PubMed: 23359221]
38. Vashist SK, Schneider EM, Luong JH, Commercial smartphone-based devices and smart applications for personalized healthcare monitoring and management. Diagnostics (Basel) 4, 104–128 (2014). [PubMed: 26852680]
39. Lerner RM, Limitations in the use of dielectric interference filtesr in wide angle optical receivers. Appl Opt 10, 1914–1918 (1971). [PubMed: 20111227]
40. Chung H, Dai T, Sharma SK, Huang YY, Carroll JD, Hamblin MR, The Nuts and Bolts of Low-level Laser (Light) Therapy. Ann Biomed Eng 40, 516–533 (2012). [PubMed: 22045511]
41. Wei JCJ, Edwards GA, Martin DJ, Huang H, Crichton ML, Kendall MAF, Allometric scaling of skin thickness, elasticity, viscoelasticity to mass for micro-medical device translation: from mice, rats, rabbits, pigs to humans. Sci Rep-Uk 7 15885 (2017).
42. He K, Zhang X, Ren S, Sun J, Deep Residual Learning for Image Recognition. Proc IEEE Conf Comput Vis Pattern Recognit, 770–778 (2016).
43. Russakovsky O, Deng J, Su H, Krause J, Satheesh S, Ma S, Huang Z, Karpathy A, Khosla A, Bernstein M, Berg AC, Fei-Fei L, ImageNet Large Scale Visual Recognition Challenge. Int J Comput Vis 115, 211–252 (2015).
44. Choi JS, Zhu Y, Li H, Peyda P, Nguyen TT, Shen My.Y., Yang YM, Zhu J, Liu M, Lee MM, Sun SS, Yang Y, Yu HH, Chen K, Chuang GS, Tseng HR, Cross-Linked Fluorescent Supramolecular Nanoparticles as Finite Tattoo Pigments with Controllable Intradermal Retention Times. ACS Nano 11, 153–162 (2017). [PubMed: 27997116]
45. Anderson JM, Shive MS, Biodegradation and biocompatibility of PLA and PLGA microspheres. Adv Drug Deliver Rev 28, 5–24 (1997).
46. Zhong H, Chan G, Hu YJ, Hu H, Ouyang DF, A Comprehensive Map of FDA-Approved Pharmaceutical Products. Pharmaceutics 10 (2018).
47. Sardana K, Ranjan R, Ghunawat S, Optimising laser tattoo removal. J Cutan Aesthet Surg 8, 16–24 (2015). [PubMed: 25949018]
48. Zhong HZ, Wang ZB, Bovero E, Lu ZH, van Veggel FCJM, Scholes GD, Colloidal $CuInSe_2$ nanocrystals in the quantum confinement regime: synthesis, optical properties, and electroluminescence. J Phys Chem C 115, 12396–12402 (2011).
49. Liu Y, Yao D, Shen L, Zhang H, Zhang X, Yang B, Alkylthiol-Enabled Se Powder Dissolution in Oleylamine at Room Temperature for the Phosphine-Free Synthesis of Copper-Based Quaternary Selenide Nanocrystals. J Am Chem Soc 134, 7207–7210 (2012). [PubMed: 22515639]
50. Li ZC, Yao W, Kong L, Zhao YX, Li L, General Method for the Synthesis of Ultrastable Core/Shell Quantum Dots by Aluminum Doping. J Am Chem Soc 137, 12430–12433 (2015). [PubMed: 26389704]
51. Ding K, Jing LH, Liu CY, Hou Y, Gao MY, Magnetically engineered Cd-free quantum dots as dual-modality probes for fluorescence/magnetic resonance imaging of tumors. Biomaterials 35, 1608–1617 (2014). [PubMed: 24239108]
52. Schneider CA, Rasband WS, Eliceiri KW, NIH Image to ImageJ: 25 years of image analysis. Nat Methods 9, 671–675 (2012). [PubMed: 22930834]
53. Mishra R, Bhattacharyya TK, Maiti TK, Theoretical analysis and simulation of SU-8 microneedles for effective skin penetration and drug delivery. IEEE Sensor, 1769–1772 (2015).

54. Rad ZF, Faraji Rad Z, Nordon RE, Anthony CJ, Bilston L, Prewett PD, Arns JY, Arns CH, Zhang L, Davies GJ, High-fidelity replication of thermoplastic microneedles with open microfluidic channels. Microsyst Nanoeng 3 17034 (2017). [PubMed: 31057872]

55. Huang KZ, Xu ZL, King I, Lyu MR, Campbell C, Supervised Self-taught Learning: Actively Transferring Knowledge from Unlabeled Data. Ieee Ijcnn, 481-+ (2009).

56. Quattoni A, Collins M, Darrell T, Transfer learning for image classification with sparse prototype representations. Proc Cvpr Ieee, 2300–2307 (2008).

57. Tzeng SY, Guarecuco R, McHugh KJ, Rose S, Rosenberg EM, Zeng Y, Langer R, Jaklenec A, Thermostabilization of inactivated polio vaccine in PLGA-based microspheres for pulsatile release. J Control Release 233, 101–113 (2016). [PubMed: 27178811]

58. Allen PM, Bawendi MG, Ternary I-III-VI quantum dots luminescent in the red to near-infrared. J Am Chem Soc 130, 9240–9241 (2008). [PubMed: 18582061]

59. Jing LH, Kershaw SV, Li Y, Huang X, Li Y, Rogach AL, Gao M, Aqueous Based Semiconductor Nanocrystals. Chem Rev 116, 10623–10730 (2016). [PubMed: 27586892]

60. Li LA, Pandey A, Werder DJ, Khanal BP, Pietyga JM, Klimov VI, Efficient Synthesis of Highly Luminescent Copper Indium Sulfide-Based Core/Shell Nanocrystals with Surprisingly Long-Lived Emission. J Am Chem Soc 133, 1176–1179 (2011). [PubMed: 21207995]

61. Reiss P, Protiere M, Li L, Core/Shell Semiconductor Nanocrystals. Small 5, 154–168 (2009). [PubMed: 19153991]

62. Computer code associated with Biocompatible near-infrared quantum dots delivered to the skin by microneedle patches to record vaccination.

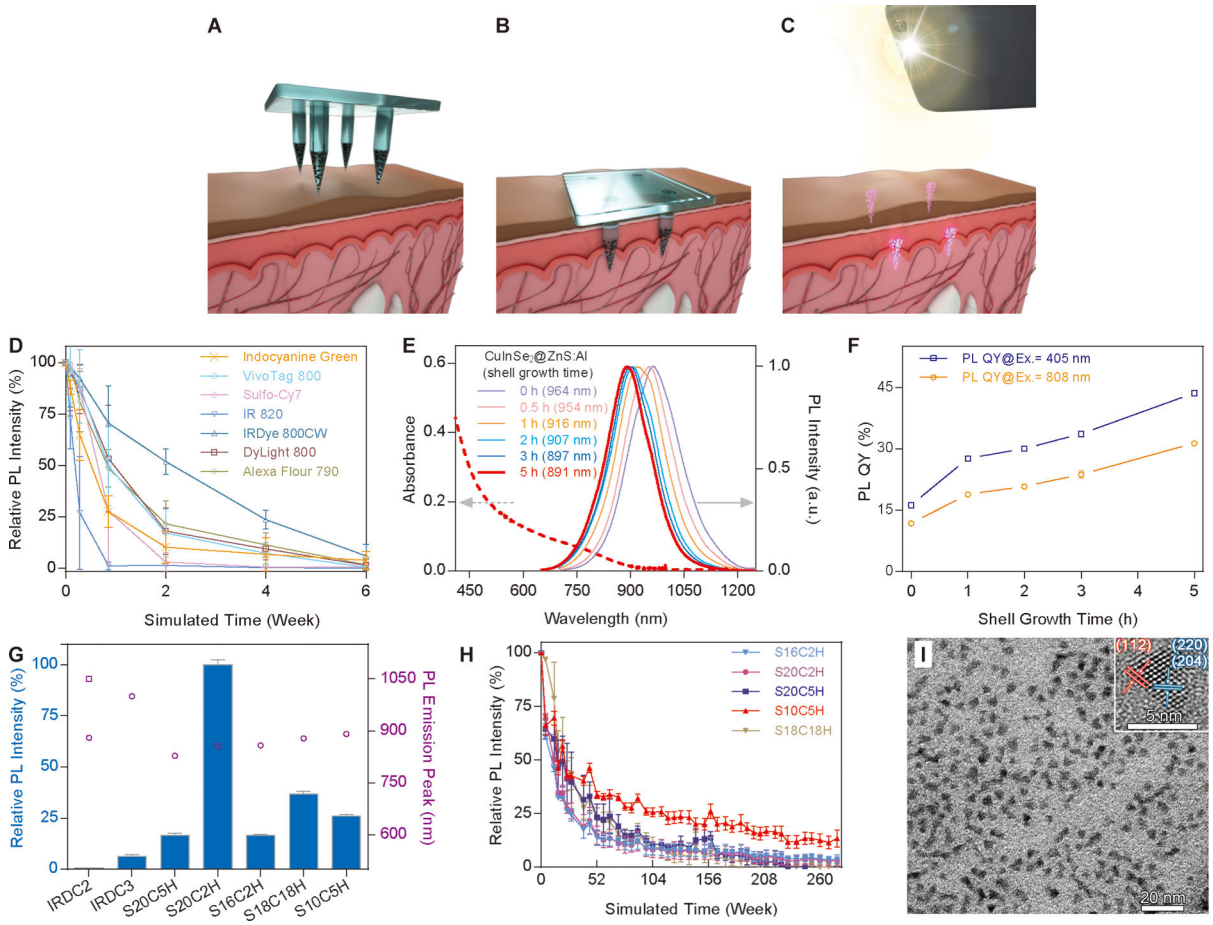

Fig. 1. Platform schematic and fluorescent probe characterization.

(A) Fluorescent microparticles are distributed through an array of dissolvable microneedles in a distinct spatial pattern. **(B)** Microneedles are then applied to the skin for two to five minutes, resulting in dissolution of the microneedle matrix and retention of fluorescent microparticles. **(C)** A NIR LED and adapted smartphone are used to image patterns of fluorescent microparticles retained within the skin. By selectively embedding microparticles within microneedles used to deliver a vaccine, the resulting pattern of fluorescence detected in the skin can be used as an on-patient record of an individual's vaccination history. **(D)** Rapid photobleaching of organic dyes covered with pigmented human skin under simulated solar light. **(E)** The emission profiles of QDs (solid lines) show a blue shift with increased shelling time. Dashed line depicts absorption by the 5 h shelling sample. Arrows indicate the relevant y-axis for excitation (left) and emission (right). **(F)** Photoluminescence quantum yield as a function of shelling time under different excitation wavelengths. **(G)** Relative photoluminescence intensity comparison of QDs with the commercial inorganic dyes IRDC2 and IRDC3 (blue bars) and corresponding emission peaks (empty purple circles and square). **(H)** Photostability of QDs covered with pigmented human skin under simulated solar light. **(I)** Transmission electron microscopy (TEM) and high resolution TEM (inset) showing the size and crystal structure of ZnS:Al-coated $CuInSe_2$ QDs. Scale bars represent 20 nm and 5 nm, respectively. n=3 for all graphs containing error bars, error bars indicate standard deviation.

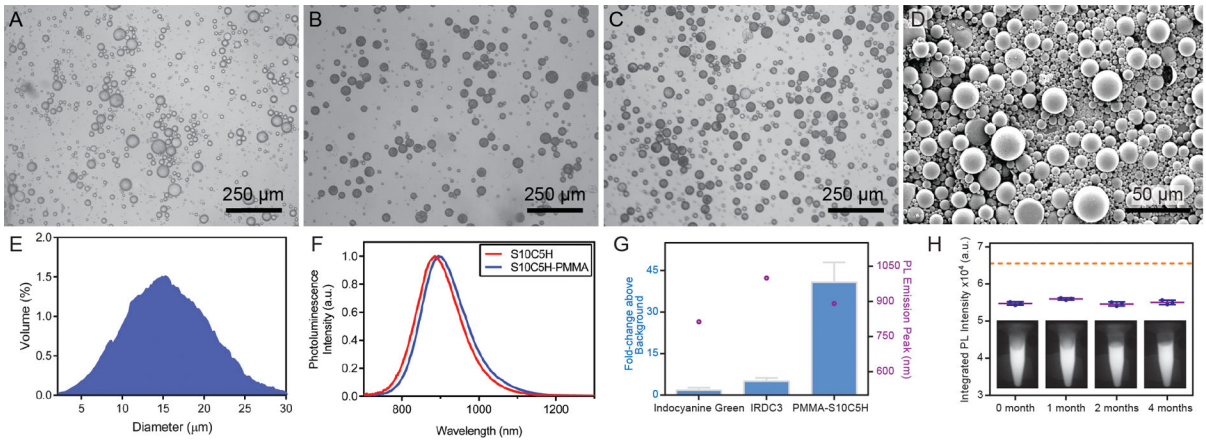

Figure 2. Encapsulation and characterization of QDs in PMMA microspheres.

Light microscopy images of PMMA microspheres loaded with **(A)** 0% w/w QDs, **(B)** 37.5% w/w QDs, and **(C)** 60% w/w QDs. Scale bar indicates 250 μm. **(D)** SEM image of PMMA microparticles containing S10C5H QDs. **(E)** Histogram of volumetric particle distribution smoothed using an eleven-frame moving window smoothing function for improved clarity, n=10^4 particles analyzed. **(F)** PL profiles of S10C5H QDs before and after PMMA encapsulation showing a minimal shift in fluorescence emission wavelength. **(G)** Relative photoluminescence intensities (blue bars) using an 850 nm long-pass filter (n=2) and emission peaks (empty purple circles). **(H)** Maintenance of photoluminescence intensity in phosphate buffered saline at 37°C over the course of months, with representative NIR images inlaid at their respective time points, $*P < 0.05$ (one-way ANOVA with Tukey's multiple comparisons). Dashed line indicates the camera saturation point. n=3 for all graphs containing error bars, error bars indicate standard deviation.

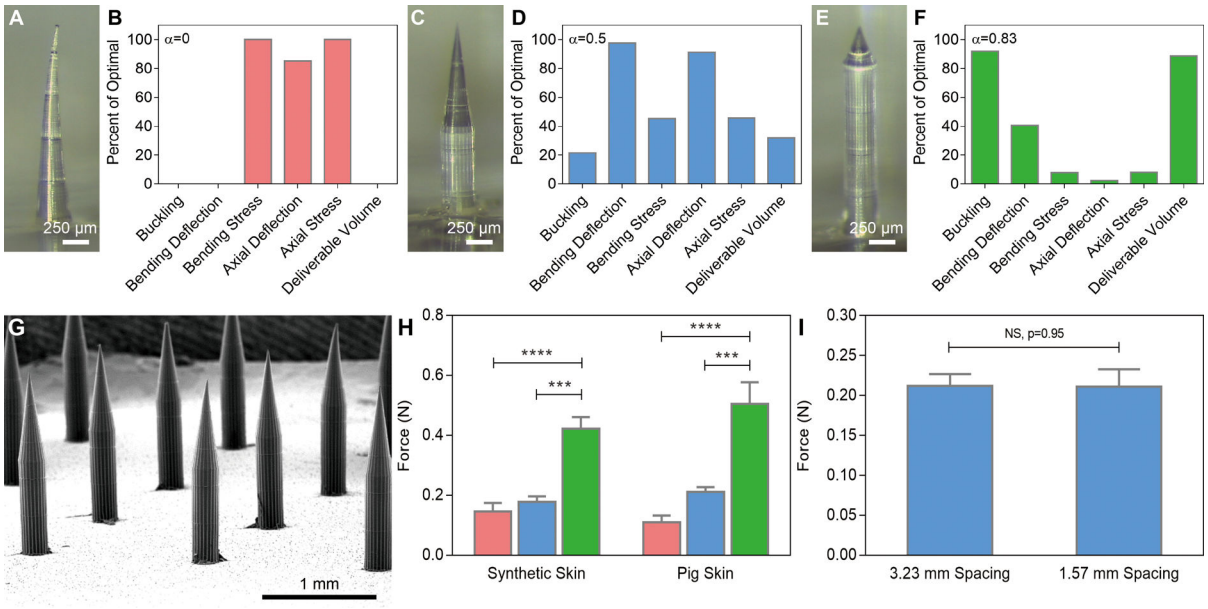

Fig. 3. Microneedle modeling, fabrication, and evaluation.

Optical images of microneedles and finite element analysis data of **(A-B)** a conical needle 1500 μm in height and 300 μm at its base; **(C-D)** a microneedle 300 μm at its base with a 750 μm cone atop a 750 μm cylinder; and **(E-F)** a microneedle 300 μm at its base with a 250 μm cone atop a 1250 μm cylinder. **(G)** SEM image of a dissolvable microneedle array based on the geometry shown in (C). (**H**) Ex vivo penetration force per needle based on microneedle geometry, n=3, ***$P < 0.001$, ****$P < 0.0001$ (one-way ANOVA with Tukey's multiple comparisons). **(I)** Spacing-independent penetration force requirements in pig skin ex vivo (Student's t-test). In (B, D, F), zero and one hundred represent the worst and best values, respectively, for each parameter for α between 0 and 1.

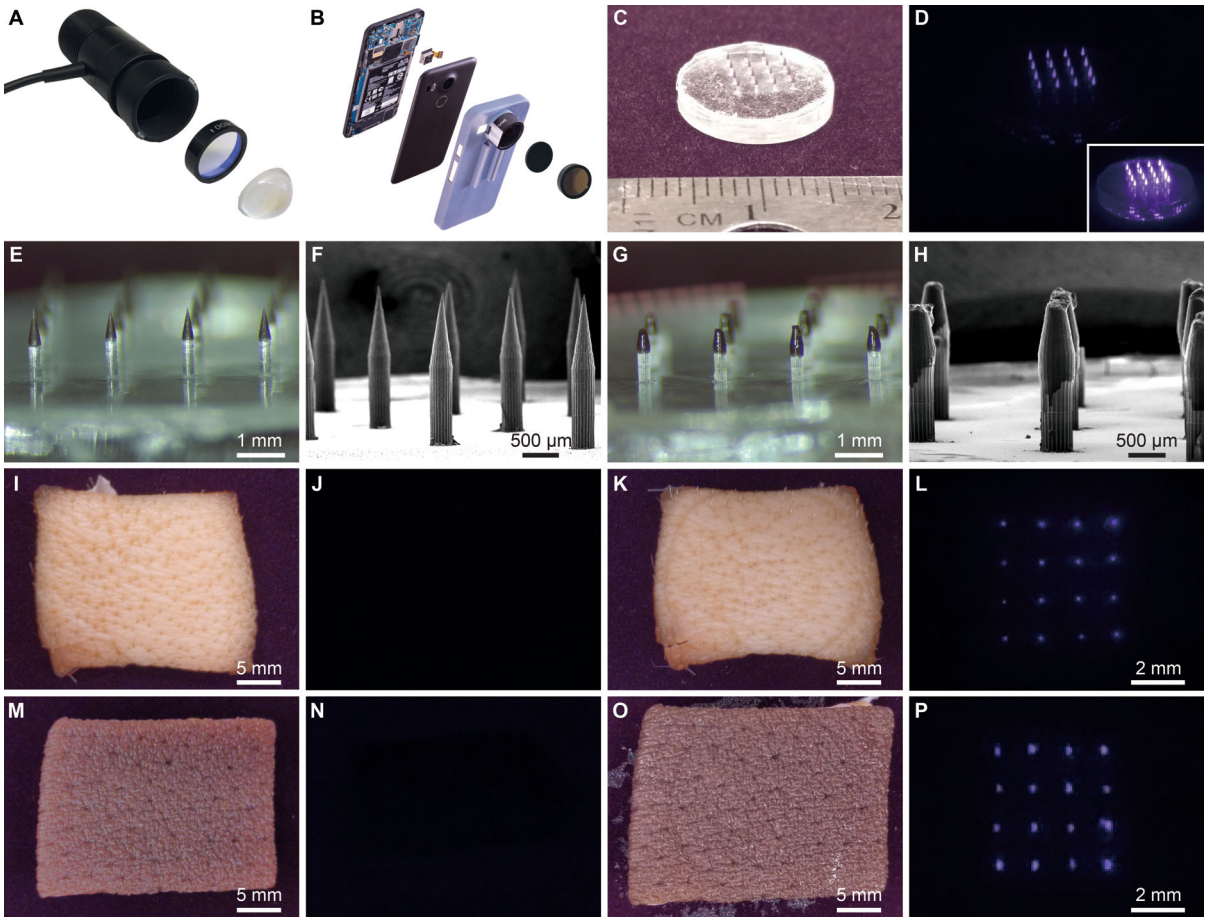

Fig. 4. Smartphone modifications and near-infrared marking detection in skin.

(A) Photograph of disassembled LED used for NIR illumination at 780 nm combined with an 800 nm short-pass filter and aspheric condenser. **(B)** Photograph of disassembled NIR imaging smartphone consisting of a Google Nexus 5x smartphone with the internal short-pass filter removed and replaced with two external 850 nm long-pass filters set in a 3D-printed phone case. Images of a 16-needle microneedle patch containing PMMA-encapsulated QDs were collected with the adapted smartphone under ambient indoor lighting **(C)** without the 850 nm long-pass filters and **(D)** with the pair of 850 nm long-pass filters under LED illumination from the same distance. Inset shows an image at a higher exposure. **(E)** Optical and **(F)** SEM images of fluorescent microparticle-loaded microneedles prior to skin application. **(G)** Optical and **(H)** SEM images of microneedles after administration to explanted pig skin. Adapted smartphone images of pig skin prior to microneedle application **(I)** without and **(J)** with 850 nm long-pass filters. Adapted smartphone images of pig skin after application **(K)** without and **(L)** with 850 nm long-pass filters. Adapted smartphone images of pigmented human skin prior to microneedle application **(M)** without and **(N)** with the 850 nm long-pass filters. Smartphone images of human skin after application **(O)** without and **(P)** with the 850 nm long-pass filters. Note: Scale bars in NIR-filtered images are approximate with (J, L, N, P) taken at about the same distance. Components in panels (A) and (B) cropped for clarity.

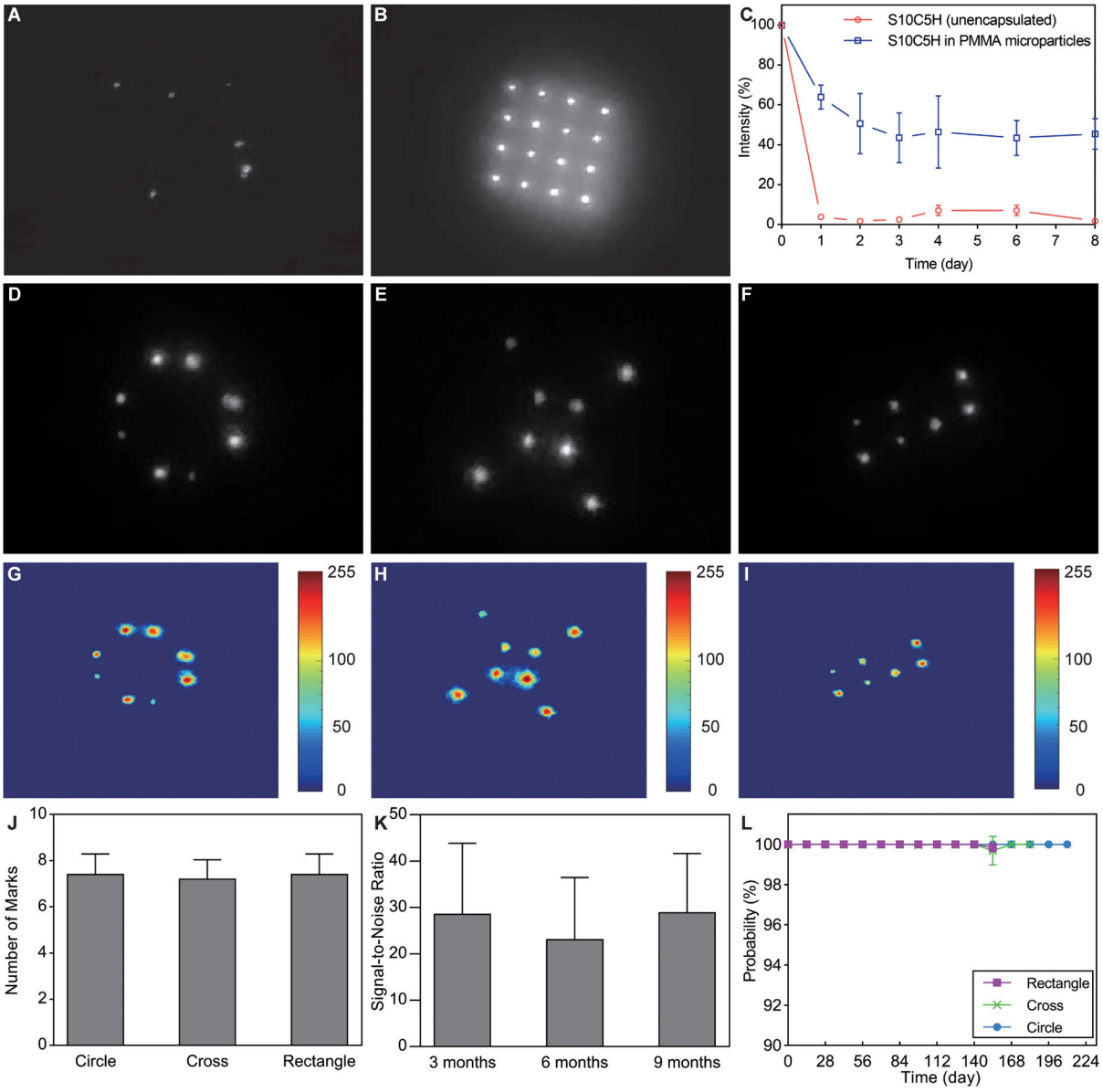

Fig. 5. In vivo imaging of NIR patterns in rodent skin.

Administration site after the delivery of a 4×4 microneedle patch containing **(A)** unencapsulated QDs or **(B)** PMMA-encapsulated QDs. **(C)** Short-term study of signal intensity after microneedle application of unencapsulated or PMMA-encapsulated QDs to rat skin, n=4. Images of **(D)** circle, **(E)** cross, and **(F)** rectangle patterns imaged 24 weeks after administration of PMMA-encapsulated QDs to rats. Log-scale color maps of the same **(G)** circle, **(H)** cross, and **(I)** rectangle patterns shown in (D-F). **(J)** Number of markings detected 24 weeks post-administration, n=5. **(K)** Quantification of signal-to-noise ratio for the circle pattern showing no changes between 12, 24, and 36 weeks, n=15 (one-way ANOVA with Tukey's multiple comparisons). **(L)** Graph showing the average probability of the machine learning algorithm (all patterns correctly detected), n=5. Grayscale images extracted from red channel of the adapted smartphone-generated RGB image.

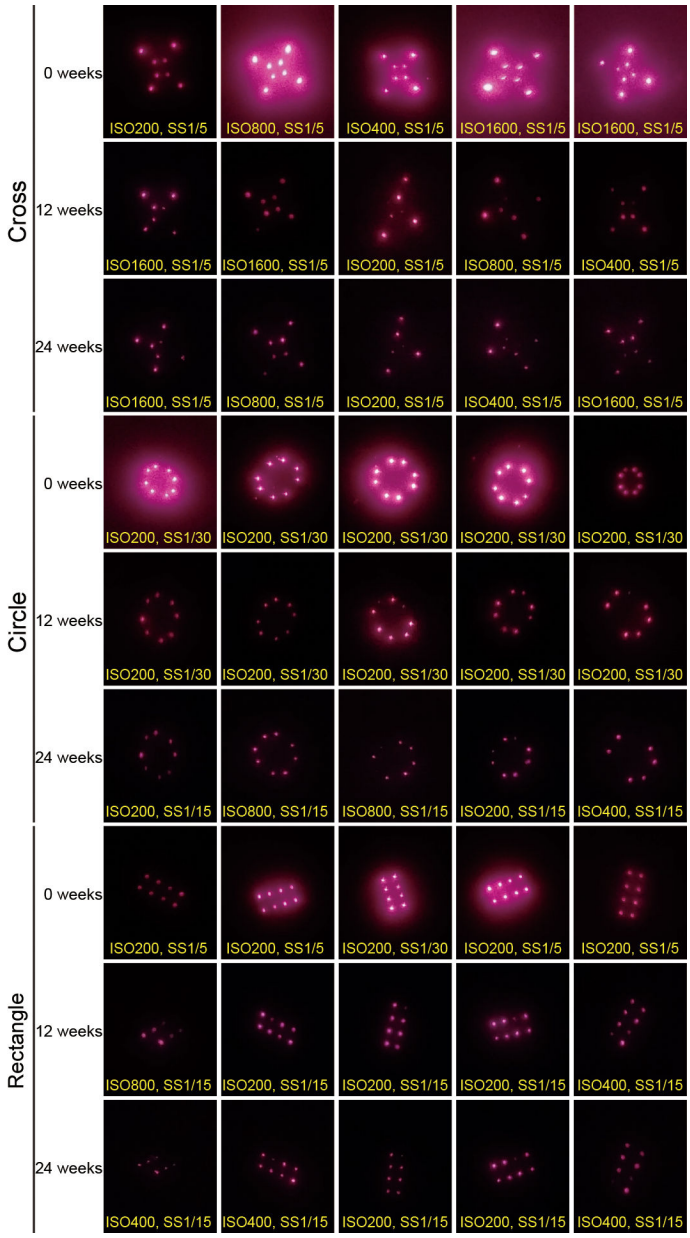

Fig. 6. Longitudinal imaging of NIR markings in rodent skin.

Cropped, but otherwise raw, smartphone images collected from a fixed distance showing the intradermal NIR signal from PMMA-encapsulated QDs delivered via microneedle patches on rats 0, 12, and 24 weeks after administration. The text at the bottom of each image indicates the image collection settings ISO density and shutter speed (SS) in seconds.

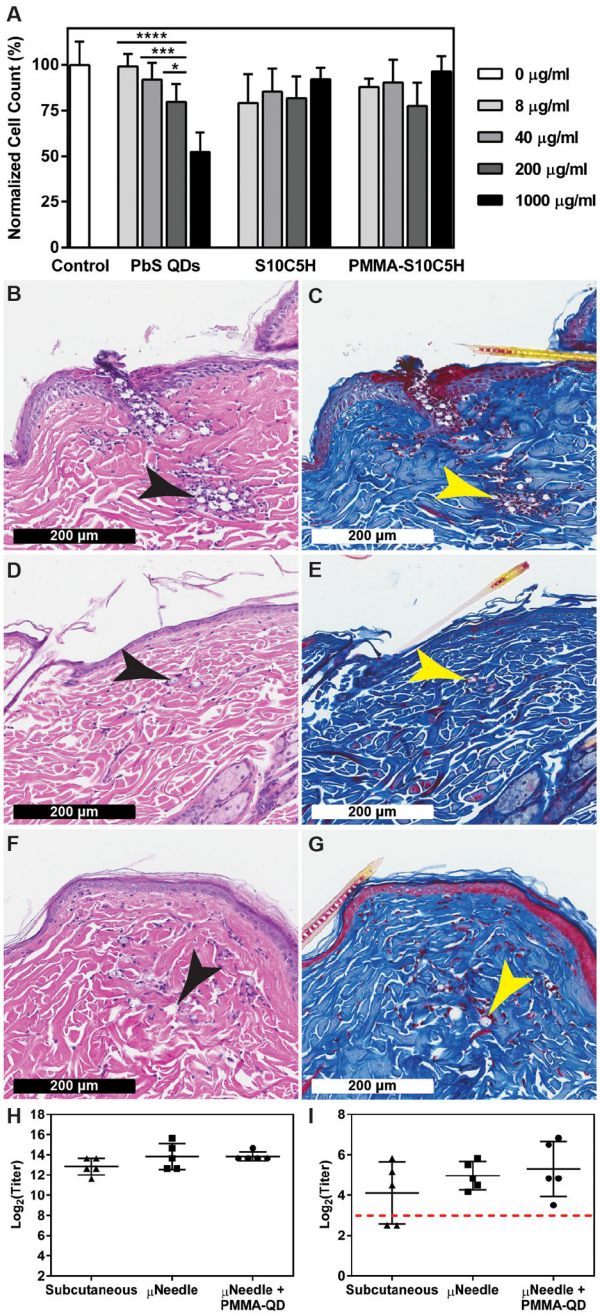

Fig. 7. Biological response to PMMA-encapsulated quantum dots.

(A) In vitro cytotoxicity of commercially-available PbS QDs compared to unencapsulated and PMMA-encapsulated S10C5H QDs over 24 hours in a mouse macrophage cell line (Raw 264.7). n=3, $*P < 0.05$, $***P < 0.001$, $****P < 0.0001$ (two-way ANOVA with Tukey's multiple comparisons). Representative histological samples collected from rats receiving microneedle-delivered PMMA particles containing S10C5H QDs **(B, C)** one day, **(D, E)** two weeks, and **(F, G)** four weeks after administration stained with hematoxylin and eosin or Masson's trichrome, respectively. Arrows indicate the location of microparticles. **(H)** Total anti-poliovirus type 2 IgG antibody titers and **(H)** neutralizing poliovirus type 2

antibody titers showing no differences after three doses of type 2 inactivated poliovirus vaccine delivered via subcutaneous injections or microneedles with or without PMMA-encapsulated QDs, n=5. Dashed line indicates the threshold above which humans are considered immune.